Editors' Suggestion

Moiré Fringe Induced Gauge Field in Photonics

Wenhui Wang,[1,*] Wenlong Gao,[1,*,†] Xiaodong Chen,[2,*] Fulong Shi,[2] Guixin Li,[3] Jianwen Dong,[2,‡] Yuanjiang Xiang,[4,§] and Shuang Zhang[1,5,6,¶]

[1]School of Physics & Astronomy, University of Birmingham, Birmingham B15 2TT, United Kingdom
[2]School of Physics & State Key Laboratory of Optoelectronic Materials and Technologies, Sun Yat-sen University, Guangzhou 510275, China
[3]Department of Materials Science and Engineering, Southern University of Science and Technology, Shenzhen 518055, China
[4]School of Physics and Electronics, Hunan University, Changsha 410082, China
[5]Department of Physics, University of Hong Kong, Hong Kong, China
[6]Department of Electrical & Electronic Engineering, University of Hong Kong, Hong Kong, China

(Received 23 May 2020; accepted 23 October 2020; published 13 November 2020)

We realize moiré fringe induced gauge field in a double-layer photonic honeycomb metacrystal with mismatched lattice constants. Benefitting from the generated strong effective gauge field, we report direct measurement of the band diagrams of both Landau level flat bands and intermagnetic-domain edge states. Importantly, we observe the correlation between the momentum and orbital position of the Landau modes, serving as an evidence of the noncommuteness between orthogonal components of the momentum. Without complicated time driving mechanics and careful site-by-site engineering, moiré superlattices could emerge as a powerful means to generate effective gauge fields for photonics benefiting from its simplicity and reconfigurability, which can be applied to nonlinearity enhancement and lasing applications at optical frequencies.

DOI: 10.1103/PhysRevLett.125.203901

When two periodic patterns with mismatched lattice constants are combined, they form a beating pattern with longer range quasiperiodicity, which are called moiré superlattices (MS). The atomic scale MS have been utilized to modify the electronic properties and have been exploited for generating strong electron correlations, Hofstadter spectrum, fractional quantum Hall effect and van Hove singularities [1–5]. Very recently, it was discovered that magic-angle twisted bilayer graphene possess flat band and function as correlated Mott insulators, providing a gateway towards high temperature superconductors [6,7]. Theoretical studies have attributed the flat band of magic-angle bilayer graphene to the effective gauge field EGF [8–10]. In optoelectronics, the versatility of the MS in tuning the electronics band structures has facilitated the interactions of electrons with photons resulting in formation of nanoscale waveguiding and IR plasmons [11]. Despite the normally small relative angle between the bilayer van der Waals heterostructures, the electronic band structure is radically altered, resulting in various novel physical properties such as topological helical states [12,13] and topological crystalline insulators [14].

MS have been also explored in classical systems. In photonics, MS have been used to create effective gratings to control the diffractions of light [15]. Plasmonic double layer MS are found to induce a strong circular dichroism for light [16]. Very recently, flat bands in double layer photonic crystals are explored for their capabilities in localizing and delocalizing light [17]. Meanwhile, effective gauge field (EGF) has been a long-sought effect in both quantum and classical systems such as photonics and acoustics. Using methods including straining and deforming the lattice, giant EGF has been created in graphene [18–21]. In photonics and optomechanical systems with EGF, nonreciprocal phase shift, Lorentz force, Landau energy levels have been revealed [22–30]. Lasing utilizing the Landau level modes has also been proposed in photonic graphene [31]. In acoustic systems with EGF, Landau levels were found in phononic crystals with gradual deformations of the crystal inclusions [32], and chiral zero mode was observed in acoustic Weyl systems [33].

Here we report the creation of EGF, or more specifically, effective magnetic field (EMF), in a moiré bilayer metacrystal (MBM) [Fig. 1(a)], which leads to experimental observation of the band diagrams of the photonic Landau level modes and intermagnetic-domain edge states in the microwave regime. Our microwave near field measurements provide a direct and definite evidence of the gauge field induced flat band and the surface states. In addition, we directly observe the correlation between the momentum and the orbital location of the Landau modes, which indicates noncommuteness between the orthogonal components of momentum introduced by the EMF. Our findings provide a new platform for studying moiré pattern related effects in classical wave systems and may find applications in flat band lasing, nonlinear optics.

The bilayer metacrystal consists of two parallel two-dimensional hexagonal-lattice metallic ring metacrystals

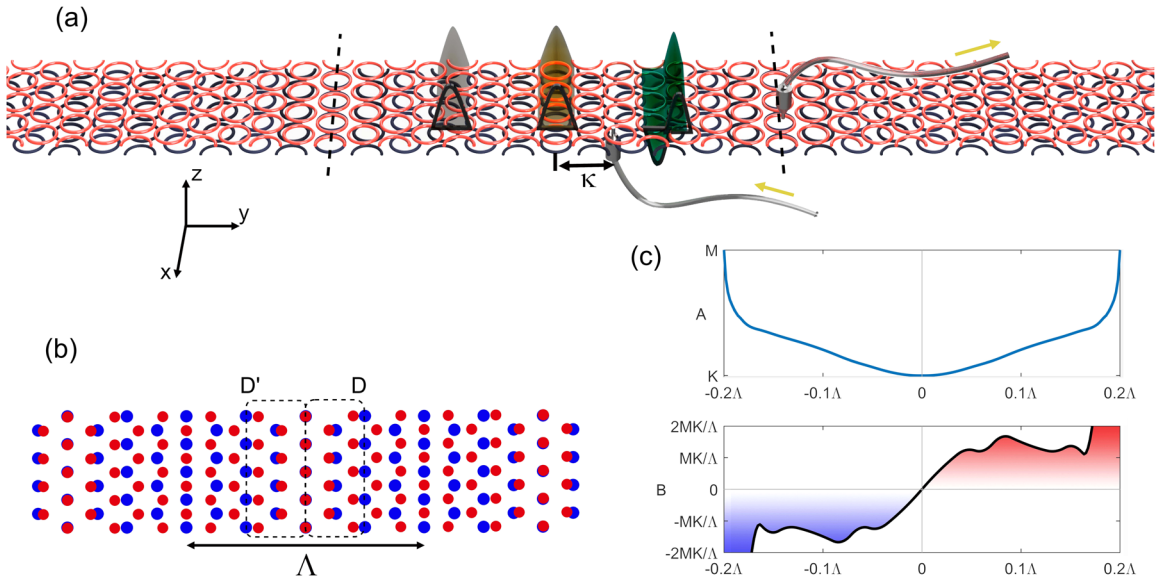

FIG. 1. (a) Illustration of the double layer moiré pattern bilayer metacrystal. The metallic rings in the upper and lower layer are colored in red and dark blue, respectively. The red layer has a normal hexagonal lattice whose lattice constant is $a = 5$ mm. The lower (blue) layer is stretched in the y direction relative to the upper layer, and a moiré superlattice is formed with the periodicity indicated by the black dashed lines. κ is the deviation of the excitation dipole from the moiré pattern center. The gray and the green wave forms represent the Landau level flat band modes (0th and ± 1th order) and the orange one in the middle represents the interdomain surface states. These modes are localized in the y direction and propagating in the x direction. (b) Illustration of the 1D moiré pattern formed between two lattice-constant mismatched metacrystals. The red and blue dots represent the metallic rings in the upper and lower layers, respectively. Two effective magnetic field domains D and D' are identified. The moiré quasiperiodicity is Λ. (c) Top: Gauge field represented by the location of the Dirac cones measured locally within one moiré pattern. Bottom: the distribution of the effective magnetic field given by the gradient of the gauge field. The sign switching leads to formation of two magnetic domains in each moiré periodicity.

separated by a thin dielectric layer ($\varepsilon_r \approx 10$). A relative lattice constant mismatch in the y direction is introduced to the bilayer system to form MBM, with a quasiperiodicity Λ given by $l_y^2/\delta l$ in which δl is the difference in their lattice constants along the y direction. An illustration of the MBM whose metallic rings represented by colored dots are given in Fig. 1(b). As will be shown later, due to the spatially varying local misalignment between the two layers in the MBM, an inhomogeneous gauge field is introduced, leading to generation of effective magnetic field for each Dirac cone [Fig. 1(c)].

To understand the origin of the artificial magnetic field, we first study two identical hexagonal metacrystals aligned to each other. The primitive vector of each layer has a length of 5 mm and the inner and outer radius of the rings are 2.1 and 2.4 mm, respectively. Each metacrystal layer alone supports spoof surface plasmons [34–39], which exhibit Dirac cones around 12.5 GHz at K and K' points of the Brillouin zone due to the C_{3v} symmetry [40–42] (Supplemental Material [43], Fig. S1). By positioning the two metacrystals close to each other separated by a thin dielectric layer, they strongly interact with each other and form hybridized modes. The Dirac cones experience a strong energy splitting due to the near-field interaction. Single Dirac cone dispersion similar to that of a single layer is found at 12.65 GHz (Supplemental Material [43], Fig. S1). The conical dispersions, measured by the near-field scanning system, are in excellent agreement with numerical simulations [Fig. 2(a)]. In the experiments, the excitation and receiving microwave antennas are placed on opposite surfaces of the metacrystal system [Fig. 1(a)]. The lower excitation dipole is fixed at the center of the sample, while the upper receiving dipole performs a 2D grid raster scanning. After a 2D Fourier transformation of the measured field, we obtain the equifrequency contours (EFC) at different frequencies. The Dirac cone dispersion of the EFC are clearly visualized (Supplemental Material [43], Fig. S1) through the shrinking and expanding of the EFC when the frequency sweeps through the Dirac cone.

When a relative shift Δ is introduced in y between the two layers [Fig. 2(b)], the MBM experiences a symmetry reduction from C_{3v} to C_{2h} that shifts the Dirac cones along the $K(K') - M$ high symmetry line [Fig. 2(c)], rather than opening topological valley gaps [44–49]. The Dirac cone dispersion can be fully described by a low energy linear Hamiltonian that can be derived from the C_2 rotational symmetry and the parity-time-reversal symmetry (Supplemental Material [43], Note 1):

$$\mathscr{H} = v_x(k_x - \delta k)\sigma_x + v_y k_y \sigma_y + (Tk_x + \omega_0)I, \quad (1)$$

where ω_0 is the frequency of the Dirac points, $v_{x,y}$ the fermi velocities in the x (y) directions, T the tilting parameter

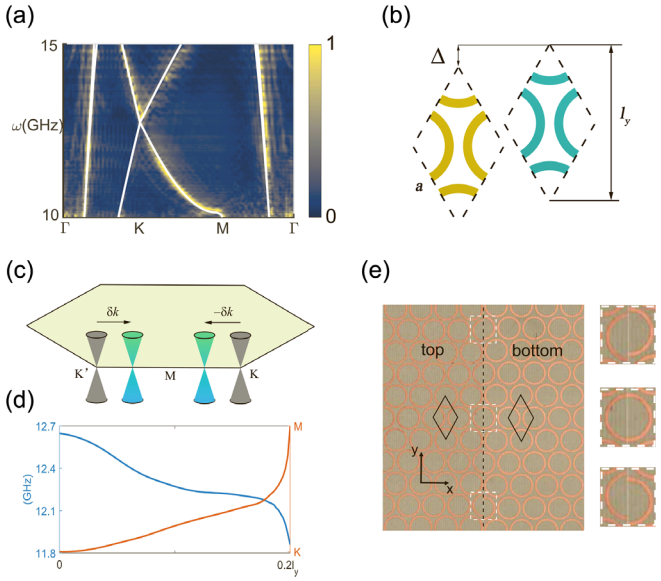

FIG. 2. (a) Experimental (color map) and numerical (white solid lines) results of the Dirac cone dispersion in the double layer metacrystal. (b) Illustration of the relative shift between the top and bottom layers. (c). Illustration of the shift of Dirac cones along the $K(K')-M$ high symmetry line. (d). Numerically extracted Dirac cone's frequency and position in the Brillouin zone vs the relative shift l_y between the top and bottom layers. (e) Side-by-side pictures of the top and the bottom metacrystal with 2.5% mismatch, separated by the black dashed line. The unit cells (black solid lines) are mismatched in the y direction, hence introducing a dislocation away from the center. Enlarged views of the dashed square areas are given on the right-hand side of the picture.

[40], δk the location of the Dirac cone that plays the role of the gauge field. All the above parameters can be retrieved from the band structure obtained by full wave simulation. The numerically extracted location and ω_0 of the Dirac points are given in Fig. 2(d). Note that beyond $\Delta = 0.2l_y$, the two Dirac points annihilate each other, and a band gap is formed.

The moiré fringe is equivalent to a periodic nonuniform shift Δ between the two layers as a function of y. The system has a mirror symmetry M_y at locations where the two layers are perfectly aligned, the EGF $\vec{A}_x$ is, hence, symmetric about this mirror plane. Therefore, for each Dirac point the moiré periodicity can be separated into two magnetic domains [D ($y>0$) and D' ($y<0$), respectively, in Fig. 1(b)] with positive and negative EMF [Fig. 1(c)]. The EMF satisfies $B_K(y) = -B_K(-y) = -B_{K'}(y) = B_{K'}(-y)$, where $B_{K(K')}(y)$ is the EMF of the Dirac points originally located at $K(K')$. Note that the domains only partly cover the MS, while the Dirac cones annihilate each other further away from the magnetic domain wall (moiré center), resulting in formation of a band gap. The EMF, however, is nonuniform in each domain because the positions of the Dirac points in the Brillouin zone are not strictly linear functions of Δ.

To observe the Landau levels experimentally, a MBM sample is prepared with a mismatch $\delta l/l_y = 2.5\%$ and a quasiperiodicity 346.4 mm. Snapshots of the top and bottom layers of the MBM are given side by side in Fig. 2(e). The field distribution is measured with the excitation dipole located at several locations with different displacements (κ) from the magnetic domain wall [Fig. 1(a)]. Because of the lack of translational symmetry in the y direction, k_x remains the only good quantum number. By combining all the measurement results at different excitation positions, the full dispersions of the photonic landau levels are obtained [Fig. 3(a)], which are in excellent agreement with that obtained by full wave simulation [Fig. 3(b)]. The band structure shows relatively flat bands of double degeneracy around the middle of the Brillouin

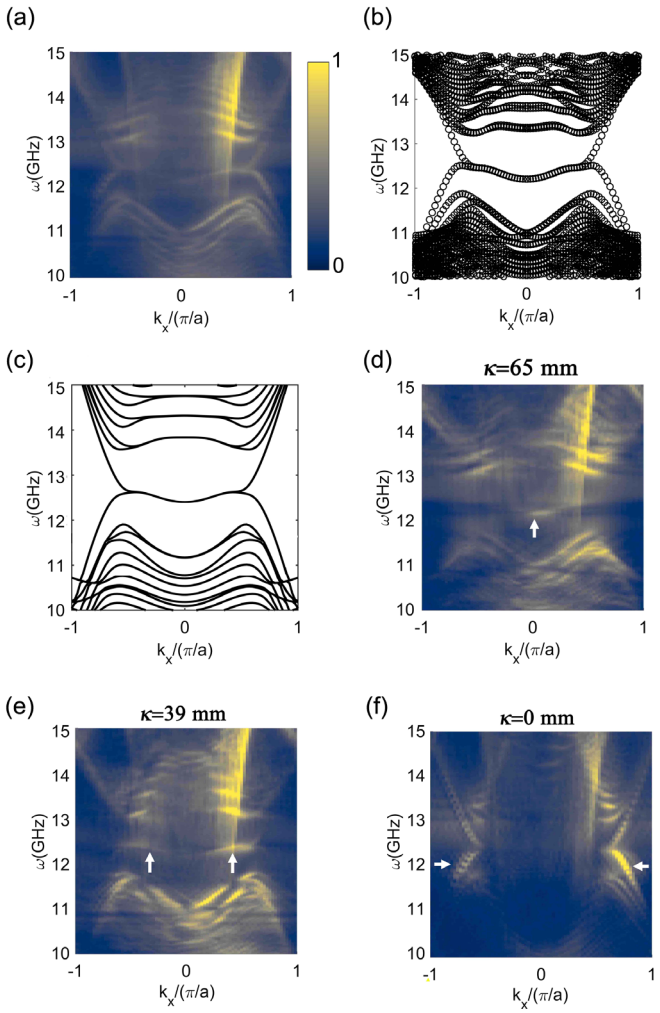

FIG. 3. (a) The overall band diagram by combining the measurements at different locations of the excitation dipole. (b) Numerically simulated band diagram of the moiré pattern metacrystal. (c) Theoretical band diagram calculated from the quadratic effective Hamiltonian. (d,e,f) Measured band diagrams when the excitation dipole is placed at 65 mm (d), 39 mm (e) and 0 mm (f) away from the center of the moiré pattern.

zone. At large k_x, the two modes split and acquire a large positive and negative slope, respectively. We show the experimental results of $\delta l/l_y = 8\%$ in the Supplemental Material [43], Note 3. Note that the Landau level modes remain even under much smaller moiré periodicity (Ref. [43], Note 5).

Next, we show that the observed Landau levels can be explained by the gauge field present in Eq. (1). Because of merging and annihilation of the two Dirac points and formation of a band gap at locations far from the moiré center, a linear Dirac Hamiltonian that only accounts for a single Dirac cone is insufficient to describe the whole system. Instead, a quadratic Hamiltonian is utilized to take into account the shift and annihilation of both Dirac cones:

$$\mathscr{H} = (\Omega_0 + \beta k_x^2)I + (E - \alpha k_x^2)\sigma_x + v_y k_y \sigma_y, \qquad (2)$$

where $\alpha, \beta, E, \Omega_0$ and v_y as functions of Δ, hence y. Derivation of the quadratic Hamiltonian from the linear Hamiltonian and the retrieval of the parameters are detailed in Supplemental Material [43], Note 2. Specifically, the gauge fields for the two Dirac points are given as $\pm\sqrt{E/\alpha}$, respectively. The numerically calculated spectrum based on the Hamiltonian Eq. (2) is presented in Fig. 3(c), which nicely captures the main feature of the Landau levels including the doubly degenerate flat bands, confirming the moiré-fringe-induced EMF as the origin of the flat bands. The double degeneracy originates from the two symmetrical Landau level orbitals residing in the two magnetic domains D and D' within each moiré period Λ. When k_x approaches the Brillouin zone boundary, the Landau level orbitals in each magnetic domain gradually move towards the magnetic wall, resulting in coupling between them and, consequently, an energy splitting and a large dispersion in the Landau levels. The correlation between the orbital location in the y direction and k_x can be revealed by the microwave near-field scanning experiment.

As shown in Figs. 3(d)–3(f), for the excitation dipole with κ equals 0, 39, and 65 mm, different parts of the band structure are excited preferentially. More specifically, with a particular location of the excitation dipole, only the modes with orbitals strongly overlapping with the excitation position can be efficiently excited. For each Landau level, these modes are centered at a particular k_x [marked by the white arrows in Figs. 3(d)–3(f)], indicating the presence of correlation between k_x and the orbital center in the y direction. This can be understood by a simple harmonic oscillator model, wherein the location of the potential minimum is determined by k_x [50]. As shown in Figs. 4(a) and 4(b), for deviations of 65 and 39 mm, we observe localized states centered around the excitation dipole due to the diminishing group velocity, representing the almost flat band states around $k_x = 0$ and $k_x = 0.4\pi/a$.

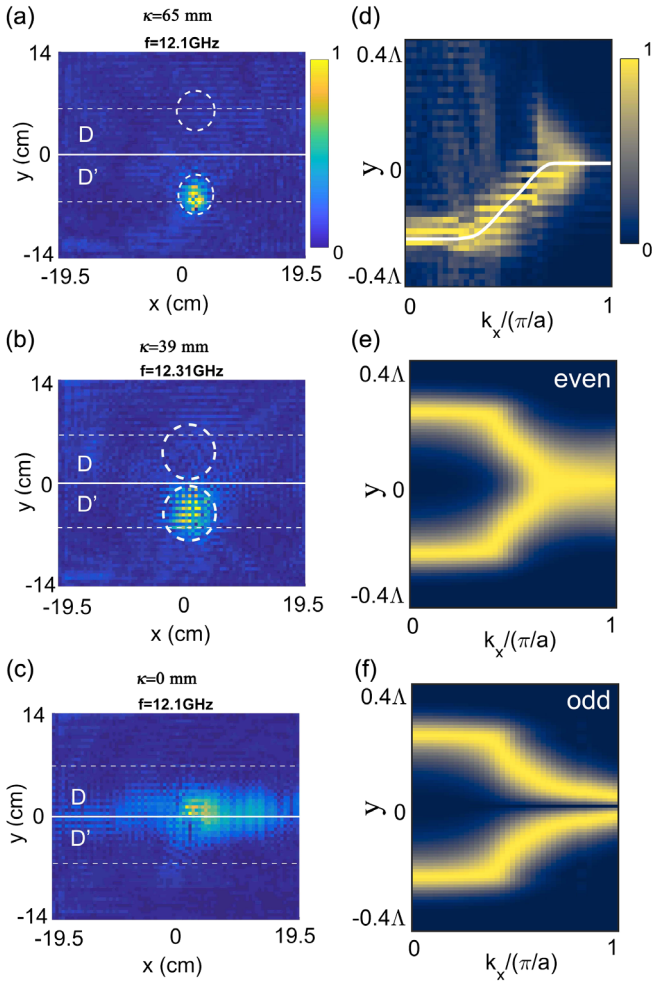

FIG. 4. (a)–(c) Real space field distributions with various excitation dipole positions corresponding to Fig. 3 (d)–(f) (d) Correlation between the experimentally extracted 0th Landau level mode profile with k_x. White solid line is the maximum of the wave function solved by effective Hamiltonian model. (e)–(f) The even and odd modes' magnitude profile vs k_x calculated by the effective model.

On the other hand, when the dipole is placed right at the MBM's domain wall ($\kappa = 0$) [Fig. 4(c)], the real space field distribution reveals an interdomain guided mode propagating in x, but confined in y.

This correlation is further illustrated by the experimental data of eigenfield distributions extracted for various k_x [Fig. 4(d)] (Supplemental Material [43], Note 4). For small k_x, the orbitals are located far from the domain wall, where the local relative shift between the two metacrystal layers is around $0.2l_y$ and the Dirac points are expected to meet at the M point. Consequently, the orbitals have negligible interactions and are doubly degenerate in frequency. As k_x increases, the orbitals in each magnetic domain move towards the domain wall, dictated by the k_x dependent potential minima in the Landau gauge. When k_x approaches the location of the original Dirac point ($2\pi/3a$) the orbitals

strongly interact with each other, forming odd and even modes (defined by E_x) at different frequencies. In experiments, the even mode extracted from the measurement data is illustrated in Fig. 4(d) using the lower frequency branch after the two Landau levels split in frequency, while the odd mode is described in the Supplemental Material [43], Fig. S7. The measured y—k_x correlation fits well with the theoretical result obtained using Eq. (2) [Fig. 4(e)] and that obtained from the full wave simulation (Supplemental Material [43], Fig. S8). Finally, for the sake of completeness we also show the theoretically calculated eigenfield distribution for the odd mode [Fig. 4(f)], which only shows noticeable difference from that of the even mode at large k_x when the field distribution is close to the domain wall.

In conclusion, we have realized effective magnetic fields in moiré bilayer metacrystals, observed the corresponding photonic Landau levels, and demonstrated the correlation between momentum and orbital location. The spoof plasma modes employed in the construction of the Dirac points allow strong interaction between the layers, hence creating a strong effective gauge field. Our experiments provide a direct and definite evidence of the Landau level zero bands and the interdomain surface states in the moiré pattern system and thus provide a platform for studying moiré pattern effects in classical wave systems. Our finding may find various applications in photonics, such as flat band lasing and enhancement of nonlinear optical effects.

S. Z. acknowledges support from the European Research Council Consolidator Grant (TOPOLOGICAL), Horizon 2020 Action Project Grant No. 734578 (D-SPA), the Royal Society and Wolfson Foundation. J. D. acknowledges support from the National Natural Science Foundation of China (Grant No. 11761161002) and Natural Science Foundation of Guangdong Province (Grant No. 2018B030308005). Y. X acknowledges support from the National Natural Science Foundation of China (Grant No. 11874269).

*These authors contributed equally to this work.
†bhamwxg334@gmail.com
‡dongjwen@mail.sysu.edu.cn
§xiangyuanjiang@126.com
¶s.zhang@bham.ac.uk

[1] K. Kim, A. DaSilva, S. Huang, B. Fallahazad, S. Larentis, T. Taniguchi, K. Watanabe, B. J. LeRoy, A. H. MacDonald, and E. Tutuc, Proc. Natl. Acad. Sci. U.S.A. **114**, 3364 (2017).
[2] X. Liu, Z. Hao, K. Watanabe, T. Taniguchi, B. I. Halperin, and P. Kim, Nat. Phys. **15**, 893 (2019).
[3] L. Wang, Y. Gao, B. Wen, Z. Han, T. Taniguchi, K. Watanabe, M. Koshino, J. Hone, and C. R. Dean, Science **350**, 1231 (2015).
[4] G. Li, A. Luican, J. M. B. Lopes Dos Santos, A. H. Castro Neto, A. Reina, J. Kong, and E. Y. Andrei, Nat. Phys. **6**, 109 (2010).
[5] D. I. Indolese, R. Delagrange, P. Makk, J. R. Wallbank, K. Wanatabe, T. Taniguchi, and C. Schönenberger, Phys. Rev. Lett. **121**, 137701 (2018).
[6] Y. Cao, V. Fatemi, S. Fang, K. Watanabe, T. Taniguchi, E. Kaxiras, and P. Jarillo-Herrero, Nature (London) **556**, 43 (2018).
[7] Y. Cao, V. Fatemi, A. Demir, S. Fang, S. L. Tomarken, J. Y. Luo, J. D. Sanchez-Yamagishi, K. Watanabe, T. Taniguchi, E. Kaxiras, R. C. Ashoori, and P. Jarillo-Herrero, Nature (London) **556**, 80 (2018).
[8] P. San-Jose, J. González, and F. Guinea, Phys. Rev. Lett. **108**, 216802 (2012).
[9] A. Ramires and J. L. Lado, Phys. Rev. Lett. **121**, 146801 (2018).
[10] J. Liu, J. Liu, and X. Dai, Phys. Rev. B **99**, 155415 (2019).
[11] S. S. Sunku, G. X. Ni, B. Y. Jiang, H. Yoo, A. Sternbach, A. S. McLeod, T. Stauber, L. Xiong, T. Taniguchi, K. Watanabe, P. Kim, M. M. Fogler, and D. N. Basov, Science **362**, 1153 (2018).
[12] P. San-Jose and E. Prada, Phys. Rev. B **88**, 121408(R) (2013).
[13] S. Huang, K. Kim, D. K. Efimkin, T. Lovorn, T. Taniguchi, K. Watanabe, A. H. Macdonald, E. Tutuc, and B. J. LeRoy, Phys. Rev. Lett. **121**, 037702 (2018).
[14] M. Kindermann, Phys. Rev. Lett. **114**, 226802 (2015).
[15] Z. Liu, Z. Du, B. Hu, W. Liu, J. Liu, and Y. Wang, J. Opt. Soc. Am. B **36**, 2810 (2019).
[16] Z. Wu, X. Chen, M. Wang, J. Dong, and Y. Zheng, ACS Nano **12**, 5030 (2018).
[17] P. Wang, Y. Zheng, X. Chen, C. Huang, Y. V. Kartashov, L. Torner, V. V. Konotop, and F. Ye, Nature (London) **577**, 42 (2020).
[18] F. Guinea, M. I. Katsnelson, and A. K. Geim, Nat. Phys. **6**, 30 (2010).
[19] P. Nigge, A. C. Qu, É. Lantagne-Hurtubise, E. Mårsell, S. Link, G. Tom, M. Zonno, M. Michiardi, M. Schneider, S. Zhdanovich, G. Levy, U. Starke, C. Gutiérrez, D. Bonn, S. A. Burke, M. Franz, and A. Damascelli, Sci. Adv. **5**, eaaw5593 (2019).
[20] C. C. Hsu, M. L. Teague, J. Q. Wang, and N. C. Yeh, Sci. Adv. **6**, eaat9488 (2020).
[21] W. Yan, W. Y. He, Z. D. Chu, M. Liu, L. Meng, R. F. Dou, Y. Zhang, Z. Liu, J. C. Nie, and L. He, Nat. Commun. **4**, 2159 (2013).
[22] L. D. Tzuang, K. Fang, P. Nussenzveig, S. Fan, and M. Lipson, Nat. Photonics **8**, 701 (2014).
[23] K. Fang, Z. Yu, and S. Fan, Nat. Photonics **6**, 782 (2012).
[24] M. C. Rechtsman, J. M. Zeuner, A. Tünnermann, S. Nolte, M. Segev, and A. Szameit, Nat. Photonics **7**, 153 (2013).
[25] D. B. Zhang, G. Seifert, and K. Chang, Phys. Rev. Lett. **112**, 150602 (2014).
[26] F. Liu and J. Li, Phys. Rev. Lett. **114**, 103902 (2015).
[27] H. Jia, R. Zhang, W. Gao, Q. Guo, B. Yang, J. Hu, Y. Bi, Y. Xiang, C. Liu, and S. Zhang, Science **363**, 148 (2019).
[28] A. Dutt, Q. Lin, L. Yuan, M. Minkov, M. Xiao, and S. Fan, Science **367**, 59 (2020).
[29] C. Brendel, V. Peano, O. J. Painter, and F. Marquardt, Proc. Natl. Acad. Sci. U.S.A. **114**, E3390 (2017).
[30] M. Schmidt, S. Kessler, V. Peano, O. Painter, and F. Marquardt, Optica **2**, 635 (2015).

[31] H. Schomerus and N. Y. Halpern, Phys. Rev. Lett. **110**, 013903 (2013).
[32] X. Wen, C. Qiu, Y. Qi, L. Ye, M. Ke, F. Zhang, and Z. Liu, Nat. Phys. **15**, 352 (2019).
[33] V. Peri, M. Serra-Garcia, R. Ilan, and S. D. Huber, Nat. Phys. **15**, 357 (2019).
[34] A. P. Hibbins, B. R. Evans, and J. R. Sambles, Science **308**, 670 (2005).
[35] Z. Gao, L. Wu, F. Gao, Y. Luo, and B. Zhang, Adv. Mater. **30**, 1706683 (2018).
[36] Y. Yang, L. Jing, L. Shen, Z. Wang, B. Zheng, H. Wang, E. Li, N.-H. Shen, T. Koschny, C. M. Soukoulis, and H. Chen, NPG Asia Mater. **9**, e428 (2017).
[37] X. Shen and T. J. Cui, Laser Photonics Rev. **8**, 137 (2014).
[38] W. Sun, Q. He, S. Sun, and L. Zhou, Light Sci. Appl. **5**, e16003 (2016).
[39] S. Sun, Q. He, S. Xiao, Q. Xu, X. Li, and L. Zhou, Nat. Mater. **11**, 426 (2012).
[40] C. Hu, Z. Li, R. Tong, X. Wu, Z. Xia, L. Wang, S. Li, Y. Huang, S. Wang, B. Hou, C. T. Chan, and W. Wen, Phys. Rev. Lett. **121**, 024301 (2018).
[41] G. G. Pyrialakos, N. S. Nye, N. V. Kantartzis, and D. N. Christodoulides, Phys. Rev. Lett. **119**, 113901 (2017).
[42] M. Milićević, G. Montambaux, T. Ozawa, O. Jamadi, B. Real, I. Sagnes, A. Lemaître, L. Le Gratiet, A. Harouri, J. Bloch, and A. Amo, Phys. Rev. X **9**, 031010 (2019).
[43] See Supplemental Material at http://link.aps.org/supplemental/10.1103/PhysRevLett.125.203901 for derivation of linear Dirac Hamiltonian from symmetries, derivation and parameter retrieval of the quadratic Hamiltonian, experimental result of the 8% mismatch moiré pattern metacrystal, extraction of the Landau level eigen functions and the existence of Landau level under small Moiré periodicity.
[44] M. Ezawa, Phys. Rev. Lett. **109**, 055502 (2012).
[45] J. Noh, S. Huang, K. P. Chen, and M. C. Rechtsman, Phys. Rev. Lett. **120**, 063902 (2018).
[46] X. D. Chen, F. L. Zhao, M. Chen, and J. W. Dong, Phys. Rev. B **96**, 020202(R) (2017).
[47] F. Gao, H. Xue, Z. Yang, K. Lai, Y. Yu, X. Lin, Y. Chong, G. Shvets, and B. Zhang, Nat. Phys. **14**, 140 (2018).
[48] Y. Kang, X. Ni, X. Cheng, A. B. Khanikaev, and A. Z. Genack, Nat. Commun. **9**, 1 (2018).
[49] H. Pan, Z. Li, C. C. Liu, G. Zhu, Z. Qiao, and Y. Yao, Phys. Rev. Lett. **112**, 106802 (2014).
[50] R. B. Laughlin, Phys. Rev. B **23**, 5632 (1981).